Susorney, H. C. M., James, P. B., Johnson, C. L., Chabot, N. L., Ernst, C. M., Mazarico, E. M., Neumann, G. A., & Kinczyk, M. J. (2019). The thickness of radar-bright deposits in Mercury's northern hemisphere from individual Mercury Laser Altimeter tracks. *Icarus*, *323*, 40-45. https://doi.org/10.1016/j.icarus.2019.01.016

The thickness of radar-bright deposits in Mercury's northern hemisphere from individual Mercury Laser Altimeter tracks

Hannah C. M. Susorney[a,b], Peter B. James[c], Catherine L. Johnson[a,b], Nancy L. Chabot[d], Carolyn M. Ernst[d], Erwan M. Mazarico[e], Gregory A. Neumann[e], Mallory L. Kinczyk[f]

[a]*Department of Earth, Ocean and Atmospheric Sciences, University of British Columbia, Vancouver, BC V6T 1Z4, Canada.*
[b]*Planetary Science Institute, Tucson, AZ 85719, USA*
[c]*Baylor University, Waco TX 76798*
[d]*The Johns Hopkins University Applied Physics Laboratory, Laurel, MD 20723, USA.*
[e]*Goddard Space Flight Center, Greenbelt, MD 20771*
[f]*North Carolina State University, Raleigh, NC 27695*

Abstract

The discovery of Mercury's radar-bright deposits has expanded our understanding of volatiles in the solar system. Key to deciphering the history and origin of the radar-bright deposits is an estimate of the volume of radar-bright material that in turn requires a measure of the average thickness of the deposits. In this study we investigate changes in topography across radar-bright deposits hosted in flat-floored, complex craters using individual edited Mercury Laser Altimeter (MLA) tracks. We compare the difference in heights of radar-bright regions and non-radar-bright regions of the crater floor and the difference of similarly sized and located regions in non-radar-bright craters and show that the two populations cannot be distinguished. The similarity of topography in these two sets of craters allows an upper limit of 15 m to be placed on the thickness of the radar-bright deposits.

Keywords: Mercury, Polar Deposits, Laser Altimeter

1. Introduction

The discovery that the north and south polar regions of Mercury contain radar-bright deposits was enabled nearly 30 years ago by Earth-based radar data (Slade et al., 1992; Harmon and Slade, 1992; Butler et al., 1993; Harmon et al., 1994, 2001; Harmon, 2007; Harmon et al., 2011). These observations provided evidence that the nearest planet to the Sun may host volatile reservoirs. One of the goals of the MEercury Surface, Space ENvironment, GEeochemistry, and Ranging (MESSENGER) mission was to characterize these polar deposits to understand their nature and origin (Solomon et al., 2007). MESSENGER observations have shown that radar-bright regions exist in areas of permanent shadow, the largest of which occur within craters near Mercury's poles (e.g., Deutsch et al., 2016; Chabot et al., 2018). In addition, evidence from multiple instruments on the MESSENGER spacecraft identified water ice as the most likely source of radar-bright material (Neumann et al., 2013; Paige et al., 2013; Lawrence et al., 2013; Chabot et al., 2014, 2016).

Determining the age and origin of these deposits is important to understand the history of water-ice on Mercury. For example, it is not currently known how old the deposits are, whether the water-ice was delivered by a single impactor or many impactors, and whether the impactor(s) in question was an asteroid or a comet. To understand the origin of the deposits, a reliable estimate of their volume must be obtained. The areal extent and minimum thickness of the deposits (on the order of several radar wavelengths,

implying a depth of several meters, Black et al. (2010)) have been constrained by radar images (i.e., Harmon et al., 2011) and maps of permanent shadows (Chabot et al., 2012, 2013; Deutsch et al., 2016), but maximum thickness values have varied (Talpe et al., 2012; Eke et al., 2017; Deutsch et al., 2018). In this study, we measure the maximum thickness of the deposits using a different approach from those adopted previously and derive a new estimate for the volume of water-ice on Mercury. Hereafter, we will refer to the deposits as radar-bright deposits as we use the radar-bright areal extent in this study. Before discussing the methodology used in our study, we first review measurements to-date of the maximum ice thickness.

In Talpe et al. (2012) the thickness of the radar-bright deposits was measured using two methods with Mercury Laser Altimeter (MLA) tracks. In the first method, the surface roughness of the interiors of craters that host radar-bright deposits and the interiors of craters that do not host such deposits were compared. No differences in surface roughness between the two types of craters were found, providing no constraints on the thickness of the deposits from this method. In the second method, crater depth-to-diameter ratios of craters that host radar-bright and non-radar-bright deposits were used to place an upper estimate on the thickness of radar-bright deposits of 170 m.

More recently, Eke et al. (2017) used gridded MLA data to compare the interior topography of craters that host radar-bright deposits and craters that do not host radar-bright deposits and found excess heights associated with the craters that host radar-bright deposits of 55 ± 35 m ($1\ \sigma$). Deutsch et al. (2018) used the depth-to-diameter ratio of small craters and the assumption

that these craters pre-dated the radar-bright deposits to place an upper limit of the thickness of the deposits. By comparing the depth-to-diameter ratio of these small craters to the corresponding relationship for the general simple crater population an upper limit for the thickness of radar-bright deposits was found to be 41 +30/-14 m (1 σ).

In this study, we estimate the thickness of radar-bright deposits by comparing the topography of individual crater floors that are partially covered in radar-bright deposits and partially free of radar-bright deposits using edited MLA tracks. In the following sections, we summarize the MLA data used and how we selected craters for this analysis. We then present how the difference in height was assessed between the region of the crater floor hosting radar-bright material and the region of the floor without radar-bright material. In order to quantify the effects of natural variability in crater floor topography, we performed similar measurements using control craters that do not host radar-bright material. Finally, we discuss the results of our study and the implications for the origin of volatiles on Mercury.

2. Methods

2.1. MLA data

We used individual MLA tracks (Smith, 2017) rather than gridded MLA topography (Zuber et al., 2012) because individual MLA tracks provide higher resolution than derived gridded datasets and because gridded products suffer from interpolation in areas of sparse coverage. MLA track coverage is highest near 80°N near periapsis and where becomes increasingly more sparse towards the equator. The MLA spot to spot spacing ranges from 300–800

m depending on where in MESSENGER's orbit the measurements were obtained and the footprint size ranges from 15–100 m in diameter (Zuber et al., 2012). MLA topography is gridded at 250 m horizontal resolution and requires interpolation to fill in areas with sparse coverage. We edited individual MLA tracks (see Section 2.3) to remove topography not associated with the radar-bright deposits. We used all MLA track data but also performed the same analyses with just high threshold channel 1 data (the lowest noise channel on MLA, Cavanaugh et al. (2007)) to test the sensitivity of our results. Using high threshold channel 1 data resulted in fewer measurements (about 4% of the total MLA dataset is channel 1), but the mean values for channels 1–4 and the high threshold channel 1 were within the one standard deviation of the results. Thus the results reported here are from our analyses of the full channel 1–4 MLA data set.

2.2. Identification of craters that host radar-bright deposits

To identify craters that host radar-bright deposits for our study we first selected all craters larger than 30 km in diameter and poleward of 80°N (where the most extensive radar-bright deposits are present). This criteria resulted in a list of 11 craters. We found that 10 of the 11 craters host radar-bright deposits. However, because our goal was to compare the topography of the radar-bright and non-radar-bright regions within each crater, we retained only craters for which the floors were partially, not fully, covered in radar-bright deposits. This allows us to measure the topographic difference between the portion of the crater floors that hosts radar-bright deposits and the part that is free of such deposits, which results in an estimate of radar-bright deposit thickness. This criteria reduced the data set to 5 craters. Finally,

we checked whether any MLA tracks crossed the crater floor. Four craters (Table. 1 and Fig 1) match all of the selection criteria.

2.3. MLA track editing with MDIS images

We hand-edited MLA tracks to remove topographic returns not associated with the radar-bright deposits. While the crater floor appears superficially smooth in images and in topographic profiles of the entire crater, zooming into just the topography of the crater floor reveals substantial topographic variations even in the freshest craters observed. We projected individual MLA tracks on to a 250 meter/pixel MDIS basemap (see Fig. 2, Denevi et al. (2017)) and hand-selected and removed portions of the tracks where the topography that deviated from the crater floor such as at superposed impact craters, the central peak, the rim, and the crater walls (Fig. 3). We used the MDIS image and the MLA track together to assess where the crater floor began and ended on a given track. We edited the track in both the radar-bright and non-radar-bright region of the crater floor. From the average topography of MLA returns within the radar-bright region ($h_{radar-bright}$) and the average topography of the MLA returns in the non-radar-bright region ($h_{non-radar-bright}$) we calculated the difference in floor topography (Δh) for each MLA track that crossed the crater (Fig. 4).

$$\Delta h = h_{radar-bright} - h_{non-radar-bright} \tag{1}$$

2.4. Control Craters

To investigate the statistics of our measurement of craters that host-radar bright deposits, we used non radar-bright craters as a control dataset. We

chose craters that do not host radar-bright deposits from the crater database created by Kinczyk et al. (2018) and used a random seed to select 8 craters (Table 1) that are fresh (class 3 or above), larger than 30 km, and lie between 60°N and 80°N (the region of highest MLA track density). The freshness classification scheme is based on the crater morphology seen in images: the freshest craters are class 5 and the most degraded craters are class 1 (Kinczyk et al., 2018). We then added a polygon to the southern portion of the crater floor with a shape and extent similar to those of the radar-bright regions of craters that host radar-bright deposits (shaped similar to an orange wedge covering about 1/4 to 1/3 of the crater floor) and treated this region as if it were radar-bright. We hand-edited all tracks for the eight craters that do not host radar-bright deposits as outlined above.

3. Results

3.1. Craters that host radar-bright deposits

We calculated the mean and one standard deviation of Δh for all MLA tracks for each crater (Table. 1 and Fig. 5) and also calculated the mean and one standard deviation of all four craters, 24 ± 27 m. Table S1 and S2 give the MLA tracks used. Note that zero elevation difference—which would imply no elevation difference between radar-bright and non-radar-bright regions—is contained within one standard deviation of the combined mean.

3.2. Craters that do not host radar-bright deposits

As noted earlier, the floors of impact craters, even fresh ones, have natural topographic variations that could complicate our interpretation of topographic differences. Although we edited the MLA tracks to remove obvious

variations of topography unrelated to the radar-bright deposits, we cannot ignore the possibility that our measurements could be influenced by a natural sloping of the crater floors toward the crater walls where the deposits are generally located. To test this possibility, we identified a set of control craters without radar-bright deposits and analyzed them in the same manner as the radar-bright craters. The spread in the Δh for the eight craters that do not host radar-bright deposits was found to be similar to that for the craters that host radar-bright deposits (Fig 5). The mean Δh for all 8 craters without radar-bright deposits is 50 ± 25 m, larger than the mean Δh for the craters with radar-bright deposits. The elevation difference for the craters without radar-bright deposits obviously cannot be attributed to the presence of ice.

4. Discussion

The average Δh for the radar-bright and non-radar-bright craters are not significantly different at the 1-sigma level, and the mean Δh for the control craters is larger than the mean Δh for the craters that host radar-bright deposits. This implies that the measured 24-m difference in elevation for the craters that host radar-bright deposits likely includes a substantial contribution from the natural elevation variation of the crater floor. The sources of this natural variation include the gradual rising of topography from the center of the crater to the rim, and undulations in the floor itself.

Although the mean Δh in our radar-bright regions is less than that in our control craters, there is a large range of Δh for both sets of craters and our sample sizes are small (n=4 for partially radar-bright craters and n=8 for our

control data set). We thus address a slightly different question: given that crater floor elevations can vary considerably from crater to crater, what is the likelihood that the Δh of radar-bright regions are in fact systematically higher than the Δh of the control craters without radar-bright deposits? A Student's t-test applied to our two crater populations shows that a difference in Δh of more than 15 meters (where the Δh for the radar-bright craters is greater than that for the control craters) can be rejected at the 95% confidence level. We take this result as a plausible upper bound on the mean thickness of ice for the permanently shadowed regions included in this analysis with the caveat that our sample size is very small. This 15-m upper limit is thinner than previous estimates (Fig. 6).

We use the 15-m estimate of radar-bright material as an average thickness for all radar-bright deposits across both polar regions (with an area of 25,000 km^2 from Harmon et al. (2011)) to place an upper bound of 375 km^3 on the total volume of such deposits on Mercury. From this we calculate the mass of ice on Mercury to be 3.45×10^{17} grams (assuming the radar-bright material is pure ice with a density of 917 $\frac{kg}{m^3}$). These estimates assume that the upper bound on radar-bright material thickness derived from the four craters suitable for the analysis here is representative of all radar-bright deposits on Mercury. However, smaller craters may host thinner radar-bright deposits, especially in cases where there is only partial coverage of the crater floor, and craters where the floors are completely covered in ice (6 of the 12 craters originally investigated in section 2) may have thicker deposits. It has been proposed that the Hokusai crater could be the source of Mercury's radar-bright deposits, delivering up to 3×10^{17} g of water to Mercury, (Ernst

et al., 2018)) but one limitation of this model to date has been that the maximum mass of volatiles that could be delivered by such an impactor is on the low side of previous volume estimates. Our estimates, which are lower than previous studies, could support such a delivery method.

5. Conclusion

In this study, we investigated the thickness of radar-bright deposits on Mercury using individual MLA tracks. We found four craters that have a portion of their floor covered in radar-bright deposits and are suitable for such analysis. We also identified a control data set of eight similarly-sized craters that have no radar bright deposits. Our results demonstrate that the excess elevation associated with radar-bright deposits is difficult to distinguish from the natural variations of the crater floor, even after careful data selection and the use of the highest resolution topography data from MLA tracks (they overlap at the 1-sigma level). We find an upper limit of 15 m for the relief of the radar-bright regions, through a statistical comparison of radar-bright craters with non-radar-bright craters. The approach here is complementary to that of previous studies and the results are broadly consistent, but we find a smaller upper limit to the thickness of the radar-bright deposits. The revised thickness estimate, scaled to the full population of radar bright areas allows a calculation for the volume of such deposits (3.75×10^{17} grams). Higher-resolution laser altimetry data of Mercury from the BepiColumbo mission will allow the thickness of these deposits to be studied in greater detail and will provide information on the southern pole deposits that were not accessible with MLA data.

Acknowledgments

We would like to acknowledge the helpful review by an anonymous reviewer that improved and strengthened the paper. HCMS would like to thank G. Susorney-Seviour for comments on a draft of this paper.

References

Black, G. J., Campbell, D. B., Harmon, J. K., Sep. 2010. Radar measurements of Mercury's north pole at 70 cm wavelength. Icarus 209 (1), 224–229.

Butler, B. J., Muhleman, D. O., Slade, M. A., Aug. 1993. Mercury: Full-disk radar images and the detection and stability of ice at the North Pole. Journal of Geophysical Research: Solid Earth 98 (E8), 15003–15023.

Cavanaugh, J. F., Smith, J. C., Sun, X., Bartels, A. E., Ramos-Izquierdo, L., Krebs, D. J., McGarry, J. F., Trunzo, R., Novo-Gradac, A. M., Britt, J. L., Karsh, J., Katz, R. B., Lukemire, A. T., Szymkiewicz, R., Berry, D. L., Swinski, J. P., Neumann, G. A., Zuber, M. T., Smith, D. E., Aug. 2007. The Mercury Laser Altimeter Instrument for the MESSENGER Mission. Space Science Reviews 131 (1), 451–479.

Chabot, N. L., Ernst, C. M., Denevi, B. W., Harmon, J. K., Murchie, S. L., Blewett, D. T., Solomon, S. C., Zhong, E. D., May 2012. Areas of permanent shadow in Mercury's south polar region ascertained by MESSENGER orbital imaging. Geophysical Research Letters 39 (9).

265 Chabot, N. L., Ernst, C. M., Denevi, B. W., Nair, H., Deutsch, A. N.,
266 Blewett, D. T., Murchie, S. L., Neumann, G. A., Mazarico, E., Paige,
267 D. A., Harmon, J. K., Head, J. W., Solomon, S. C., Dec. 2014. Images of
268 surface volatiles in Mercury's polar craters acquired by the MESSENGER
269 spacecraft. Geology 42 (12), 1051–1054.

270 Chabot, N. L., Ernst, C. M., Harmon, J. K., Murchie, S. L., Solomon, S. C.,
271 Blewett, D. T., Denevi, B. W., Jan. 2013. Craters hosting radar-bright
272 deposits in Mercury's north polar region: Areas of persistent shadow de-
273 termined from MESSENGER images. Journal of Geophysical Research:
274 Planets 118 (1), 26–36.

275 Chabot, N. L., Ernst, C. M., Paige, D. A., Nair, H., Denevi, B. W., Blewett,
276 D. T., Murchie, S. L., Deutsch, A. N., Head, J. W., Solomon, S. C.,
277 Sep. 2016. Imaging Mercury's polar deposits during MESSENGER's low-
278 altitude campaign. Geophysical Research Letters 43 (18), 9461–9468.

279 Chabot, N. L., Shread, E. E., Harmon, J. K., Feb. 2018. Investigating
280 Mercury's South Polar Deposits: Arecibo Radar Observations and High-
281 Resolution Determination of Illumination Conditions. Journal of Geophys-
282 ical Research: Planets 123 (2), 666–681.

283 Denevi, B. W., Chabot, N. L., Murchie, S. L., Becker, K. J., Blewett, D. T.,
284 Domingue, D. L., Ernst, C. M., Hash, C. D., Hawkins, S. E., Keller, M. R.,
285 Laslo, N. R., Nair, H., Robinson, M. S., Seelos, F. P., Stephens, G. K.,
286 Turner, F. S., Solomon, S. C., Nov. 2017. Calibration, Projection, and
287 Final Image Products of MESSENGER's Mercury Dual Imaging System.
288 Space Science Reviews 214 (1), 2.

289 Deutsch, A. N., Chabot, N. L., Mazarico, E., Ernst, C. M., Head, J. W., Neu-
290 mann, G. A., Solomon, S. C., Dec. 2016. Comparison of areas in shadow
291 from imaging and altimetry in the north polar region of Mercury and im-
292 plications for polar ice deposits. Icarus 280, 158–171.

293 Deutsch, A. N., Head, J. W., Chabot, N. L., Neumann, G. A., May 2018.
294 Constraining the thickness of polar ice deposits on Mercury using the Mer-
295 cury Laser Altimeter and small craters in permanently shadowed regions.
296 Icarus 305, 139–148.

297 Eke, V. R., Lawrence, D. J., Teodoro, L. F. A., Mar. 2017. How thick are
298 Mercury's polar water ice deposits? Icarus 284, 407–415.

299 Ernst, C. M., and, N. C. M. C., 2018, 2018. Could the Hokusai Impact Have
300 Delivered Mercury's Water Ice? Proceedings of the Mercury: Current and
301 Future Science of the Innermost Planet Meeting, 6094.

302 Harmon, J. K., Oct. 2007. Radar Imaging of Mercury. Space Science Reviews
303 132 (2-4), 307–349.

304 Harmon, J. K., Perillat, P. J., Slade, M. A., Jan. 2001. High-Resolution
305 Radar Imaging of Mercury's North Pole. Icarus 149 (1), 1–15.

306 Harmon, J. K., Slade, M. A., Oct. 1992. Radar Mapping of Mercury: Full-
307 Disk Images and Polar Anomalies. Science 258 (5082), 640–643.

308 Harmon, J. K., Slade, M. A., Rice, M. S., Jan. 2011. Radar imagery of
309 Mercury's putative polar ice: 1999-2005 Arecibo results. Icarus 211 (1),
310 37–50.

311 Harmon, J. K., Slade, M. A., Velez, R. A., Crespo, A., Dryer, M. J., Johnson,
312 J. M., May 1994. Radar mapping of Mercury's polar anomalies. Nature
313 369 (6477), 213–215.

314 Kinczyk, M., Byrne, P., Prockter, L., Susorney, H., Barnouin, O., 2018.
315 Crater Degradation on Mercury: A Global Perspective. Proceedings of the
316 Mercury: Current and Future Science of the Innermost Planet Meeting,
317 6116.

318 Lawrence, D. J., Feldman, W. C., Goldsten, J. O., Maurice, S., Peplowski,
319 P. N., Anderson, B. J., Bazell, D., McNutt, R. L., Nittler, L. R., Pret-
320 tyman, T. H., Rodgers, D. J., Solomon, S. C., Weider, S. Z., Jan. 2013.
321 Evidence for Water Ice Near Mercury's North Pole from MESSENGER
322 Neutron Spectrometer Measurements. Science 339 (6117), 292–296.

323 Neumann, G. A., Cavanaugh, J. F., Sun, X., Mazarico, E. M., Smith, D. E.,
324 Zuber, M. T., Mao, D., Paige, D. A., Solomon, S. C., Ernst, C. M.,
325 Barnouin, O. S., Jan. 2013. Bright and Dark Polar Deposits on Mercury:
326 Evidence for Surface Volatiles. Science 339 (6117), 296–300.

327 Paige, D. A., Siegler, M. A., Harmon, J. K., Neumann, G. A., Mazarico,
328 E. M., Smith, D. E., Zuber, M. T., Harju, E., Delitsky, M. L., Solomon,
329 S. C., Jan. 2013. Thermal Stability of Volatiles in the North Polar Region
330 of Mercury. Science 339 (6117), 300–303.

331 Slade, M. A., Butler, B. J., Muhleman, D. O., Oct. 1992. Mercury Radar
332 Imaging: Evidence for Polar Ice. Science 258 (5082), 635–640.

Smith, D. E., 2017. Mercury Laser Altimeter RDR Data Release 18. NASA Planetary Data System.

Solomon, S. C., McNutt, R. L., Gold, R. E., Domingue, D. L., 2007. MESSENGER Mission Overview. Space Science Reviews 131 (1-4), 3–39.

Talpe, M. J., Zuber, M. T., Yang, D., Neumann, G. A., Solomon, S. C., Mazarico, E., Vilas, F., 2012. Characterization of the morphometry of impact craters hosting polar deposits in Mercury's north polar region. Journal of Geophysical Research: Planets 117 (E12).

Zuber, M. T., Smith, D. E., Phillips, R. J., Solomon, S. C., Neumann, G. A., Hauck II, S. A., Peale, S. J., Barnouin, O. S., Head, J. W., Johnson, C. L., Lemoine, F. G., Mazarico, E., Sun, X., Torrence, M. H., Freed, A. M., Klimczak, C., Margot, J.-L., Oberst, J., Perry, M. E., McNutt Jr, R. L., Balcerski, J. A., Michel, N., Talpe, M. J., Yang, D., Apr. 2012. Topography of the Northern Hemisphere of Mercury from MESSENGER Laser Altimetry. Science 336 (6078), 217–220.

Figures

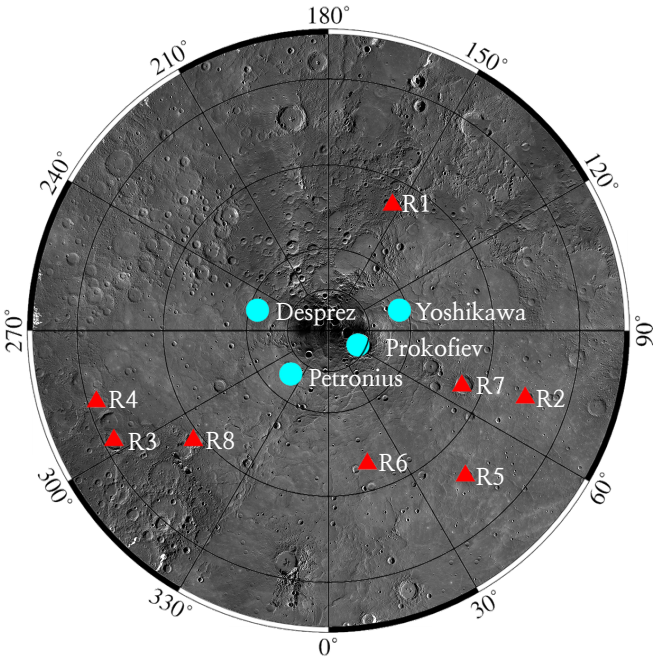

Figure 1: MDIS basemap (Denevi et al., 2017) from 55°N to 90° with longitude in degrees East. The cyan circles represent the four craters that host radar-bright deposits and the red triangles represent the 8 craters that do not host radar-bright deposits used in the study.

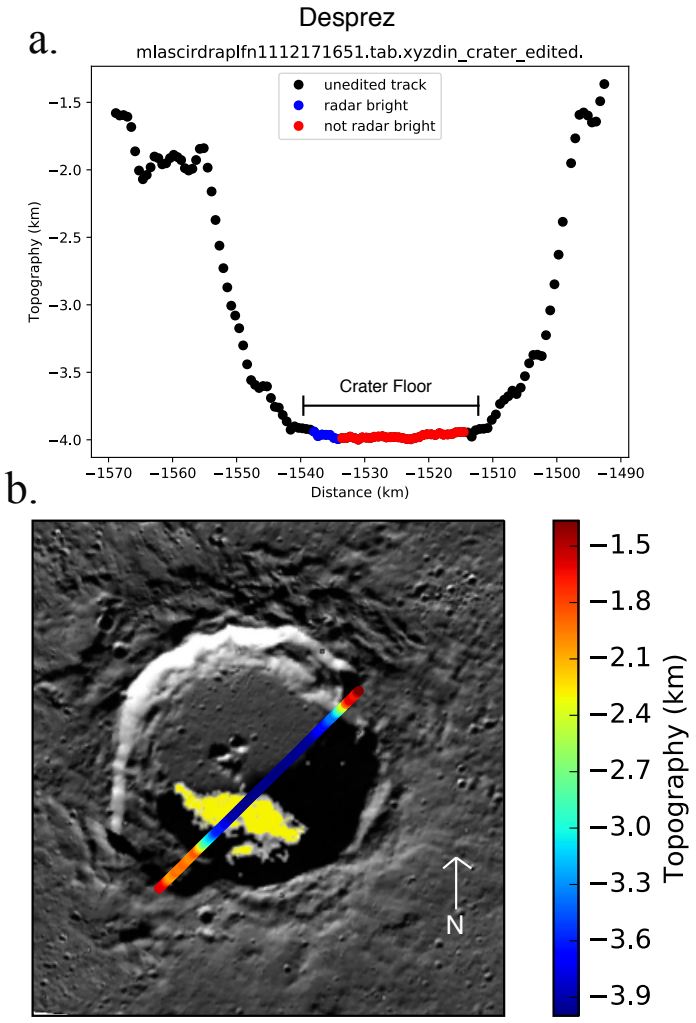

Figure 2: The 50-km diameter crater Desprez, with (a) the altimetry profile from a single MLA track and (b) the MLA track projected onto the 250 m/pixel MDIS basemap (Denevi et al., 2017). We used the MDIS image to assist in hand-editing MLA tracks: specifically to identify the part of the track crossing the radar-bright deposits (blue dots in (a)), the part of the crater floor lacking radar-bright deposits (red dots in (a)) and to identify topography unrelated to the radar-bright deposits such as central peak, crater walls, smaller impact craters (black dots in (a)).

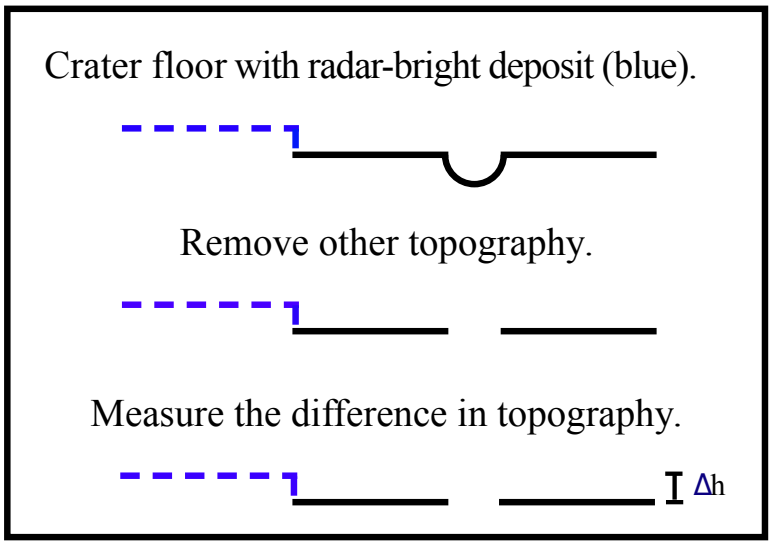

Figure 3: A schematic showing how the individual MLA tracks were filtered to remove topography unrelated to the background floor elevation and the radar bright region, to enable a measurement of the height of the radar-bright region (blue line). The difference between the crater floor that was radar-bright and the crater floor that was not radar-bright was averaged across each of their respective regions and the difference in topography was reported as Δh.

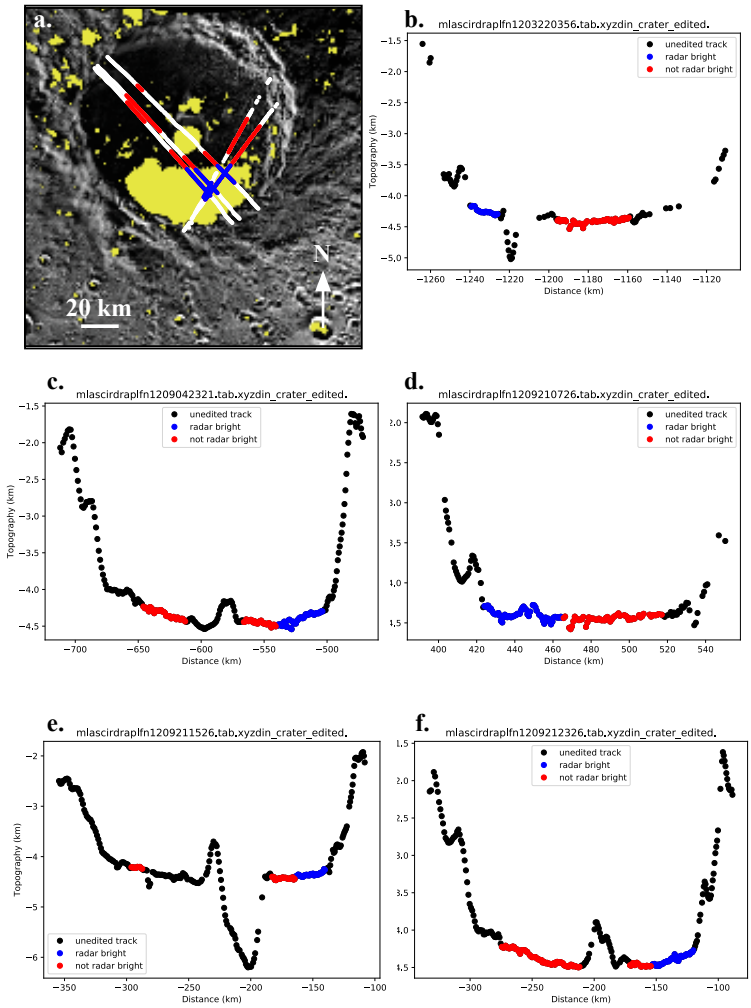

Figure 4: An MDIS base map (a) with 5 edited MLA tracks overlain for the crater Prokofiev. The yellow regions are the radar-bright regions. The white regions of the track are the portions of the track removed and the red and blue regions are the portions of the track retained after editing. The blue and red regions correspond to radar bright and non-radar bright regions respectively. The edited MLA profiles (b-f) use the same color scheme sin (a) except that the portion of the tracks that were removed are shown as black rather than white dots. Figures S1-S3 show the same information for the craters Desprez, Petronius, and Yoshikawa. Similar plots for Desprez, Petronius,Yoshikawa and R1 are in the supplementary material (Figs S1-S4).

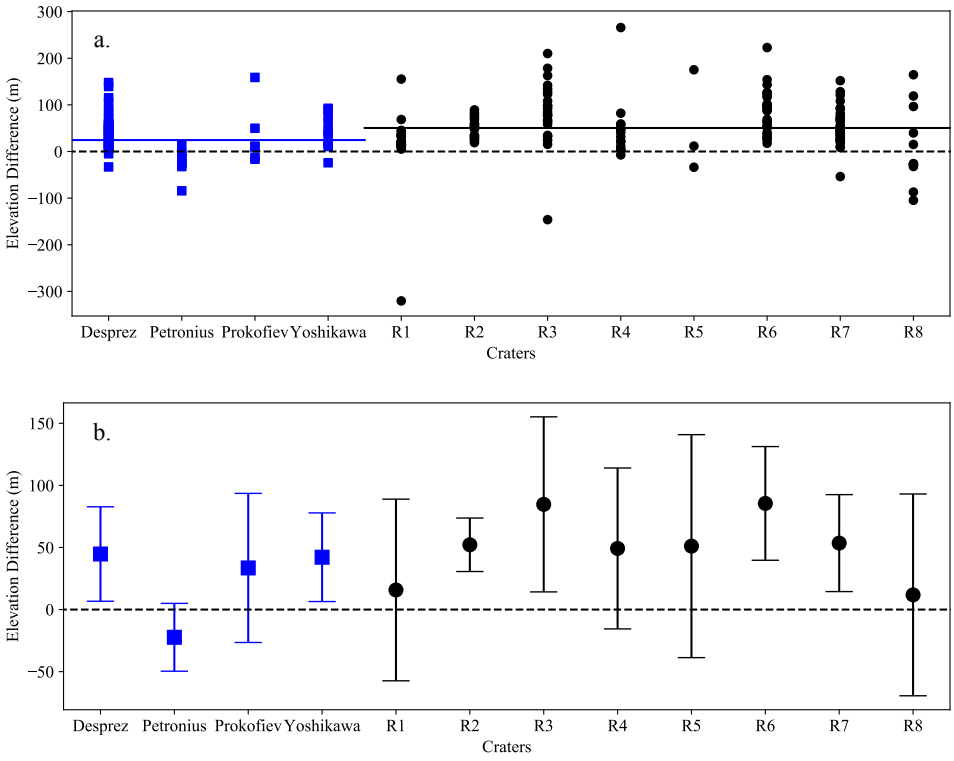

Figure 5: (a) The Δh for all MLA tracks measured for craters analyzed here that host radar-bright deposits (filled blue squares) and that do not host radar-bright deposits (filled black circles). Each point represents one Δh and the lines represent the means of the two populations. (b) The mean Δh and one standard deviation for each crater. The dotted lines in both figures represent the value if there were no difference in height between the two regions ($\Delta h = 0$).

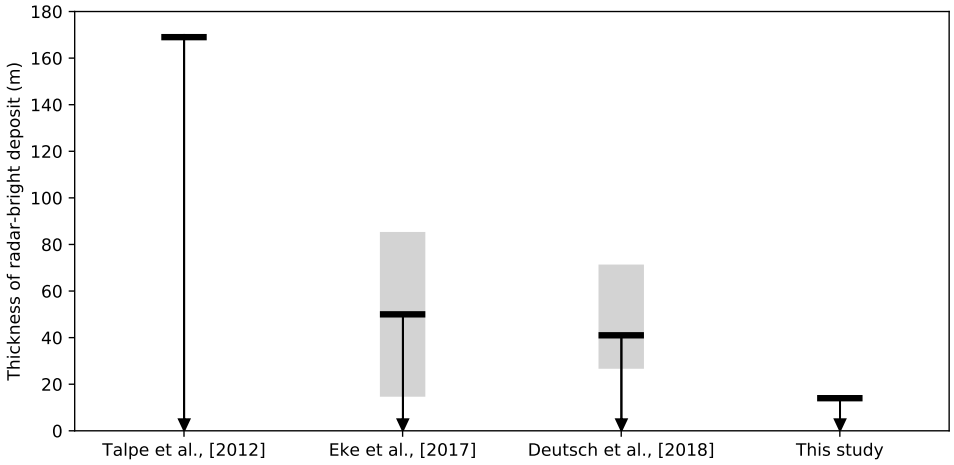

Figure 6: The range in thickness estimates for the radar-bright deposits for this study and past studies. The gray bars represent the reported error range for each study.

Tables

Table 1: Characteristics of the four radar-bright craters used in this study and the eight non-radar-bright craters used as an comparison. The freshness classification is from Kinczyk et al. (2018). The mean Δh and 1 standard deviation ($\pm$ 1 σ) are given for each crater.

Crater Name	Radar Bright?	Diameter (km)	Longitude (°E)	Latitude (°N)	Freshness Classification	Δh ($\pm 1\sigma$)	Number of MLA tracks
Desprez	yes	47	258.8	81.1	4	44 $\pm$ 38	38
Petronius	yes	36	258.7	86.0	3	-22 $\pm$ 27	8
Prokofiev	yes	112	62.9	85.8	4	36 $\pm$ 60	5
Yoshikawa	yes	30	106.5	81.2	3	42 $\pm$ 36	10
R1	no	43	153	72.9	4	16 $\pm$ 73	26
R2	no	41	71	65.0	3	52 $\pm$ 22	16
R3	no	89	297.4	61.2	3	85 $\pm$ 70	22
R4	no	41	282.7	61.0	4	49 $\pm$ 65	14
R5	no	41	43.4	66.0	3	51 $\pm$ 90	3
R6	no	45	16.3	73.2	3	85 $\pm$ 46	27
R7 (Stieglitz)	no	92	67.6	72.5	4	54 $\pm$ 39	33
R8	no	82	309.1	69.0	3	12 $\pm$ 81	11